nature materials

Article

https://doi.org/10.1038/s41563-023-01632-y

Conversion of chirality to twisting via sequential one-dimensional and two-dimensional growth of graphene spirals

Received: 27 January 2022

Accepted: 10 July 2023

Published online: 3 August 2023

Check for updates

Zhu-Jun Wang[1,2,3,21] ✉, Xiao Kong[4,5,21], Yuan Huang[6,7,21], Jun Li[1,8,21], Lihong Bao[6], Kecheng Cao[1], Yuxiong Hu[1], Jun Cai[1], Lifen Wang[6], Hui Chen[6], Yueshen Wu[1,8], Yiwen Zhang[1,8], Fei Pang[9], Zhihai Cheng[9], Petr Babor[10,11], Miroslav Kolibal[10,11], Zhongkai Liu[1,7], Yulin Chen[1,7,12,13], Qiang Zhang[14], Yi Cui[15], Kaihui Liu[16,17], Haitao Yang[6], Xinhe Bao[18], Hong-Jun Gao[6,19,20], Zhi Liu[1,3], Wei Ji[9] ✉, Feng Ding[4,5] ✉ & Marc-Georg Willinger[2] ✉

The properties of two-dimensional (2D) van der Waals materials can be tuned through nanostructuring or controlled layer stacking, where interlayer hybridization induces exotic electronic states and transport phenomena. Here we describe a viable approach and underlying mechanism for the assisted self-assembly of twisted layer graphene. The process, which can be implemented in standard chemical vapour deposition growth, is best described by analogy to origami and kirigami with paper. It involves the controlled induction of wrinkle formation in single-layer graphene with subsequent wrinkle folding, tearing and re-growth. Inherent to the process is the formation of intertwined graphene spirals and conversion of the chiral angle of 1D wrinkles into a 2D twist angle of a 3D superlattice. The approach can be extended to other foldable 2D materials and facilitates the production of miniaturized electronic components, including capacitors, resistors, inductors and superconductors.

Growth techniques that enable the production of defect-free single-layer sheets of graphene and other 2D materials have been developed considerably in recent years[1,2]. The key requirement and remaining bottleneck for the realization of graphene-based nano-electronics lies in the ability to control the electronic properties of synthetic 2D structures, and to produce them in a reproducible and consistent manner at relevant manufacturing scales. Of specific interest is the tunable interaction between electronic states and the utilization of coupling phenomena that lead to exotic electronic properties in twisted layer stacks. As predicted by theory and experimentally demonstrated on a microscale, semi-conducting, metallic and even superconducting graphene layers can be obtained depending on the stacking angle[3–6].

In this work we summarize our systematic experimental and theoretical investigations on the assisted self-assembly of twisted layer graphene. More specifically, we address the formation of graphene spirals (GSs), which are topological defects that connect individual graphene layers into a continuous, single-atom-thick helical structure that rotates around a screw dislocation axis[7,8]. Although spiralled sp^2 carbon has been observed in annealed pyrolytic graphite and anthracite[7,9,10], there have been no reports on mechanisms that enable the controlled formation of such topological defects. On the basis of real-time spatially resolved observations of graphene grown via chemical vapour deposition (CVD), we describe the formation of GSs and demonstrate how the assisted self-assembly of intertwined spirals can be used to fabricate twisted

A full list of affiliations appears at the end of the paper. ✉e-mail: wangzhj3@shanghaitech.edu.cn; wji@ruc.edu.cn; f.ding@siat.ac.cn; marc.willinger@tum.de

layer graphene with a controllable twist angle. We refer to the ancient Japanese arts of paper folding (origami) and paper cutting (kirigami), and use simple paper models to describe the experimentally observed process. It basically consists of a sequence of wrinkle formation, folding, cutting and the subsequent growth of the twisted layer graphene[11–15]. The process involves a conversion of the one-dimensional (1D) chiral angle of folded wrinkles into a three-dimensional (3D) twist angle between alternating stacked layers and, thus, provides a key to direct control of the twist angle. Our experimental observations are supported by density functional theory calculations and kinetic Monte Carlo (KMC) growth simulations. The presented sequence of graphene origami–kirigami can be implemented in a standard CVD process and is, in principle, applicable for all foldable 2D materials. This work thus presents a blueprint for the production of miniaturized electronic components, including capacitors, resistors, inductors and superconductors.

The mechanism described here for twisted layer formation was revealed through the direct observation of CVD growth initiated under controlled conditions inside the chamber of a modified environmental scanning electron microscope (ESEM)[16]. It relies on the ability to tune the balance between graphene growth and etching, and facilitates temperature-induced reconstruction of the substrate surface. In the following sections, the individual steps involved in the assisted self-assembly of twisted layer graphene are presented.

Formation of graphene wrinkles (origami)

The first step involves the local formation of graphene wrinkles and is initiated directly after completing the CVD growth of a single graphene layer that conformally covers the surface of a polycrystalline platinum (Pt) substrate. By heating the substrate beyond the initial annealing and subsequent graphene growth temperature of around 1,000 °C to a temperature of around 1,400 °C, it is possible to re-induce abnormal grain growth in the substrate[17,18]. During this process, high-surface-energy Pt grains with a pronounced stepped-surface morphology can be converted into low-energy grains that expose flat surfaces. As shown in the image sequence in Fig. 1a–d, the reconstruction of a stepped into a flat surface takes place underneath the already grown single-layer graphene by propagating grain boundaries. The reduction in surface area that accompanies the conversion of a stepped to a flat surface induces compressive strain in the graphene film[19] and the formation of wrinkles that are predominantly oriented parallel to the direction of the original step edges[13,20]. This process is illustrated schematically in Fig. 1e–g. More details regarding the surface structure are available in Extended Data Fig. 1 and Supplementary Video 1.

Wrinkle folding (origami) and tearing (kirigami)

Once the formed graphene wrinkles reach a certain height, they become mechanically unstable due to the van der Waals attractions between the sidewalls. As a consequence, the wrinkles collapse and fold towards the substrate[21]. This folding over can occur for either of the two sides, as indicated in Fig. 1g,h and visualized using paper origami–kirigami in Fig. 1i–l. Folded wrinkles can easily be identified in the ESEM images on the basis of the stepwise decrease in the secondary electron signal intensity (brightness) of each added graphene layer[22]. Folded wrinkles form a narrow three-layer graphene ribbon with an S-shaped cross-section and two tubular edges running along the folding line (of which one is buried; see the cross-section view in Fig. 1g). These tubular edges resemble structural features of single-walled carbon nanotubes, especially with respect to the high curvature at the folding edge and the defined chirality along the folding line. Owing to the random nature of folding, the wrinkles have a chance to collapse towards opposite sides and thus create a node between them. The node then tears and the graphene wrinkles up, forming two pairs of open edges (as indicated by the blue arrows in Fig. 1d, the schematic drawings in Fig. 1g,h and the paper models in Fig. 1k,l). This rupturing of wrinkles into segments folded to different sites is vital to the formation of GSs and will be discussed in more detail later.

Cracking of tubular edges (kirigami)

The next step in the assisted self-assembly of twisted layer graphene consists of gentle etching. In a well-controlled CVD process, the attachment of carbon species at low-energy growth fronts is accompanied by hydrogen etching at high-energy defective sites[23]. It is thus possible to tune the balance between growth and etching, such that highly curved graphene at the exposed tubular edge of a folded wrinkle is selectively etched (see Extended Data Fig. 2 for details). Etching along the tubular edge generates two new growth fronts: one associated with the top sheet (highlighted by the green lines in Fig. 1h,l) and one associated with the backwards-folded bottom sheet (see the origami–kirigami illustration in Fig. 1g,h and the experimental observation in Fig. 1c,d). The attachment of carbon species at these newly formed graphene edges leads to the development of low-energy zigzag edges growing on top of the original layer (see the sawtooth shape in the yellow rectangle in Fig. 1d and the green and pale blue lines in Fig. 1h, as well as in Extended Data Fig. 3). Wrinkle folding, tearing, cracking and re-growth thus result in the formation of twisted trilayer graphene. The whole process is illustrated in Fig. 1i–l using the analogy of origami–kirigami with paper[13,24].

Formation of graphene spirals

As mentioned above, the wrinkles can fold to one side or the other. It is therefore possible that wrinkles rupture up into segments that are folded towards alternating sides. This tearing (kirigami) of wrinkles results in formation of new beginning and end points (nodal points) and four additional growth fronts at the tearing edges, as illustrated in Fig. 1l using a paper model. The attachment of carbon species to these new growth fronts leads to the formation of a pair of intertwined double-layer spirals that are rotating around a common screw dislocation axis that is pinned at the nodal point. Experimental evidence for the occurrence of such processes is presented in Fig. 2a–d, and is in agreement with the KMC-based growth simulations shown in Fig. 2e–h (see Supplementary Notes 1 and 2 for details and Supplementary Video 2).

The resulting GS can be viewed as a screw dislocation formed by four graphene layers, of which two originate at each tearing edge (see also Extended Data Figs. 4 and 5). As a consequence of the opposite folding of wrinkle segments, the tearing edges at opposite nodal points always have a reversed handedness (see Extended Data Fig. 4). Since the spirals grow upwards (as confirmed using post-growth scanning probe microscopy (SPM) imaging; see Extended Data Figs. 5 and 6)[25], the handedness of the GSs can be determined through in-plane observation, as highlighted in Fig. 2b–d.

Besides the wrinkle segments, each wrinkle also has a starting and an end point (Extended Data Fig. 7a–c)[26,27]. The rupture of the tubular edge up to the apex of a wrinkle creates growth edges that meet at a nodal point. Subsequent growth results in the formation of a double spiral that winds around the tail end of the wrinkle (as shown in Extended Data Fig. 7d–f)[26,27]. Therefore, the GS at end of a graphene wrinkle can be viewed as a screw dislocation formed by two graphene layers (Extended Data Fig. 7).

1D chirality to 2D twist-angle conversion

The scanning tunnelling microscopy (STM) image recorded of a GS shows moiré superstructures formed by the two topmost graphene layers rotating around a fixed axis (Extended Data Fig. 6b). In contrast to classical screw-dislocation-based spirals, where their in-plane layer orientation is not affected[28,29], the GSs are initiated from the chirality of the wrinkle.

We used paper with printed graphene lattices to model the graphene layer and to explain how a 1D chiral angle is converted to the twisting angle of a GS (Fig. 2j–l and Supplementary Fig. 1). In this model, the chiral angle θ represents the angle of a wrinkle relative to the zigzag direction of the graphene lattice (Fig. 2j). A flattened graphene wrinkle (Fig. 2l) contains two graphene layers (Supplementary Fig. 1e,h), where the top layer has the exact same lattice orientation as the graphene basal plane, but the bottom layer has a twist angle of 2θ relative to the

https://doi.org/10.1038/s41563-023-01632-y

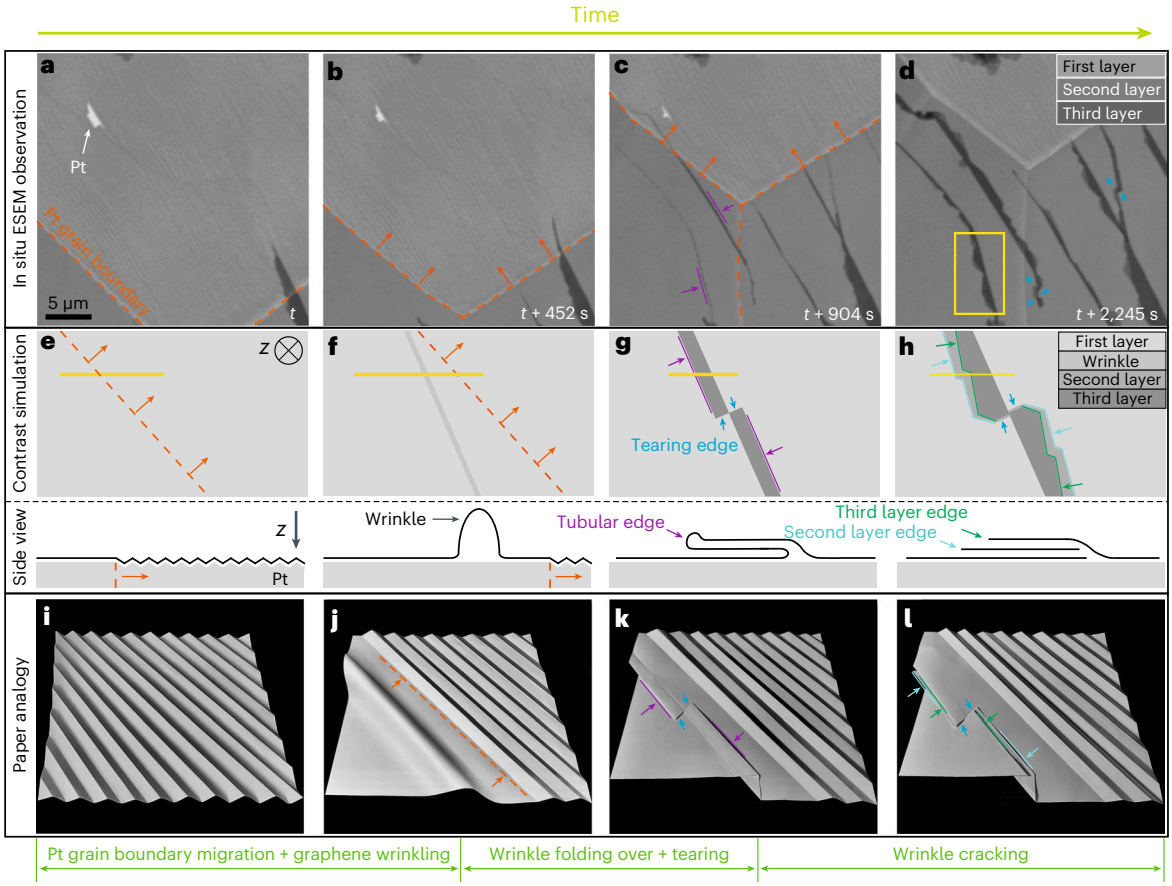

Fig. 1 | Observation and illustration of the graphene origami–kirigami process. a–d, In situ ESEM images recorded at different time points during a high-temperature annealing step (1,400 °C, 25 Pa, H_2:C_2H_4 ≈ 100:1) showing the migration of a Pt grain boundary underneath an already grown graphene layer (orange arrows). The scale bar in **a** also applies to **b**–**d**. **e**–**h**, Schematic illustrations depicting a simplified greyscale version of the process seen in **a**–**d** showing top (upper) and cross-section (lower) views. **i**–**l**, Analogous paper model showing wrinkle formation induced by reconstruction of the substrate surface, with subsequent wrinkle folding and rupture into segments that are folded to different sides (**k**,**l**). The number of stacked graphene layers in the ESEM images is apparent from the stepwise reduction in image brightness for each added layer, as shown in the greyscale key in **d** and reproduced in **e**–**h**. The propagating Pt grain boundaries are highlighted by orange dashed lines and arrows in **e** and **f**. Purple solid lines denote exposed tubular edges, while the purple arrows mark the location of the edges in **c**, **g** and **k**. Blue arrows show the tearing edges in **d**, **g**, **h**, **k** and **l**. Etching and re-growth along the exposed tubular edge results in extension of the second and third layers, as indicated, respectively, by the light blue and green solid lines and arrows in **h** and **l**. The side views in **e**–**h** represent line cuts at the locations highlighted by the yellow lines in the corresponding top views. A series of expanded images of the area highlighted by the yellow rectangle in **d** is shown in Extended Data Fig. 3.

basal plane. During the folding–cracking process, the chiral angle of the graphene wrinkle is thus increased to two times that of the twisting angle between the two graphene layers. In this case, the GSs that form at the tearing points result in a twisting angle between the adjacent layers being out-of-plane. Therefore, the transfer of the chirality of a graphene wrinkle to the twist angles of stacked graphene layers lays the foundations for designing patterns of twists in multilayer graphene along the out-of-plane direction.

As shown in Fig. 2m–p, in the case of the two graphene folds on each side of a nodal point with the same chiral angle θ, the twisting angle pattern of the GS will be in the sequence of $2\theta/0/2\theta/0/$. In the case where the two graphene folds are not parallel (Fig. 2q–t), the twisting angle pattern of the GS will be $2\theta_1/0/2\theta_2/0/$, where θ_1 and θ_2 are the chiral angles of the two graphene folds on each side of the node. Both cases can be clearly seen experimentally (Fig. 2a–c).

Coalescence of layers between two neighbouring spirals

As the graphene layers around a GS grow, the layers from neighbouring spirals will meet and coalesce. The further evolution of GSs (Fig. 3a–c and Supplementary Video 3) was imaged directly through in situ ESEM observations, where the real-time and real-space details of coalescence of the graphene layers with neighbouring GSs can be clearly seen (Fig. 3d,e). In the case of overlapped graphene layers, the images display stepwise contrast variations in the merging region (Supplementary Fig. 2)[28]. However, the contrast between individual layers is homogeneous in the merging region of the two spirals, which indicates layer-by-layer coalescence with neighbouring GSs. When two oppositely rotated growth fronts coalesce from two neighbouring GSs, their opposing Burgers vectors are annihilated, as expected for Frank–Read sources[30]; this therefore demonstrates the layer-by-layer manner of the growth of GSs.

The coalescence of each corresponding layer with the two intertwined twisted spirals is seamless, as indicated by the appearance of rounded concave corners with edges at an angle of 19° (ref. 31) (as highlighted by the orange arrow in Fig. 3e,k and Supplementary Fig. 2). This observation is favoured from an energetic point of view[32]. The seamlessness is ascribed to the oppositely rotated screw dislocations that originate on the same wrinkle with the same basal plane. The coalescence of GSs becomes more complicated if the folding axis

https://doi.org/10.1038/s41563-023-01632-y

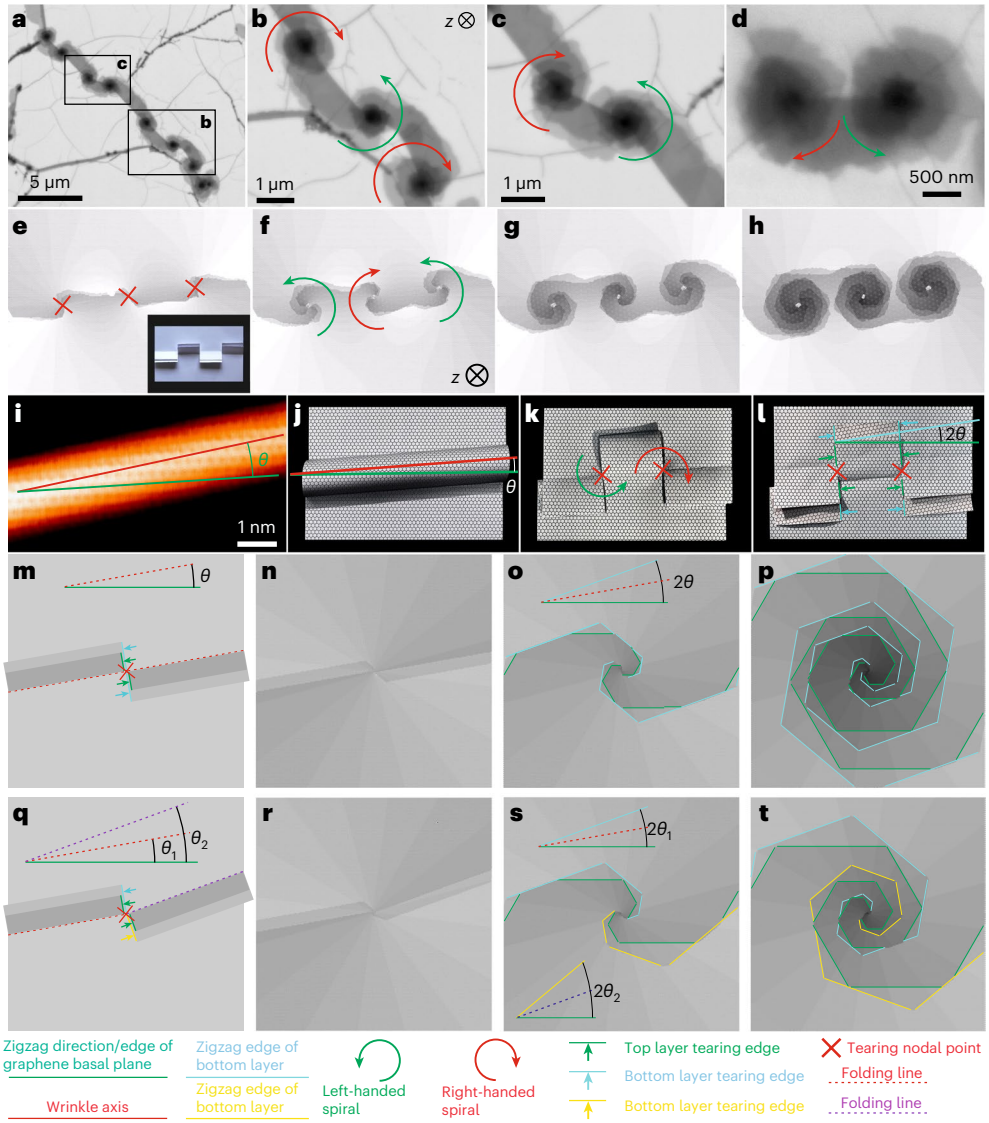

Fig. 2 | Initialization of spiral growth at torn wrinkles. a–**d**, In situ ESEM images of GSs with opposite screw dislocation handedness, with increasing magnification. The overview image (**a**) shows a chain comprised of pairs of oppositely rotated spirals, as highlighted by the black rectangles, which are shown at higher magnification in **b** and **c**. **e**–**h**, KMC simulations that reproduce the growth process at the three neighbouring spiral cores in **b**. In **e**, the inset shows a paper model of three oppositely folded wrinkle segments. **i**–**l**, Doubling of the wrinkle's chiral angle (θ) after tearing and cracking. Atomically resolved STM image (**i**) of a graphene wrinkle, the chiral angle θ of which is measured between the wrinkle axis (red line) and the zigzag direction (green line) (**i**,**j**). Wrinkle tearing, etching at the tubular edge and subsequent re-growth at opposite nodal points result in spirals of opposite handedness (**k**,**l**). In **l**, the top and bottom layers at the etched tubular edge are, due to the folding, twisted by two times the chiral angle of the original wrinkle. **m**–**t**, KMC simulations of the spiral growth processes initialized from a folded, torn and cracked nodal point in the presence of neighbouring folds with the same (**m**–**p**) and different (**q**–**t**) chiral angles. As shown in the key to the figure, the nodal points are marked by red crosses (**e**,**k**–**m**,**q**) and the left- and right-handed spirals are indicated using green and red curved arrows, respectively (**b**–**d**,**f**,**k**).

bends across the tearing nodal point, which is further described in Extended Data Fig. 8.

To verify experimentally the occurrence of the conversion from 1D chirality to the 2D twisting angle, we need first to identify the orientation of the wrinkle axis with respect to the graphene lattice. This can be done by comparing the wrinkle axis with the growth fronts of the graphene basal layer.

In Fig. 3a, the zigzag edges of the basal layer are highlighted by the blue lines, and in Fig. 3b the folding-over axis (denoted by the red line) of the wrinkle (the dark ribbon) is tilted by approximately 7° with respect to the zigzag direction (the blue line). This ~7° tilting (chiral) angle should, as exemplified in the origami–kirigami model (Fig. 2j–l and Supplementary Fig. 1), double to ~14° for the twisting angle between the top and bottom layers of the folded-over wrinkle. This was detectable even at the mesoscale (Fig. 3f).

Figure 3g,h shows the transmission electron microscopy (TEM) image of (at least six-layer) GSs exfoliated from the sample grown inside the ESEM chamber (the details are provided in Supplementary Fig. 3). Both the differently coloured hexagons in the selected area electron diffraction patterns (Fig. 3g) and the fast Fourier transform pattern of the atomic-resolution image (Fig. 3h) highlight the twisting angle of ~14° at the nano- and atomic-scales, respectively, which is consistent with the in situ ESEM observations conducted at the mesoscale.

https://doi.org/10.1038/s41563-023-01632-y

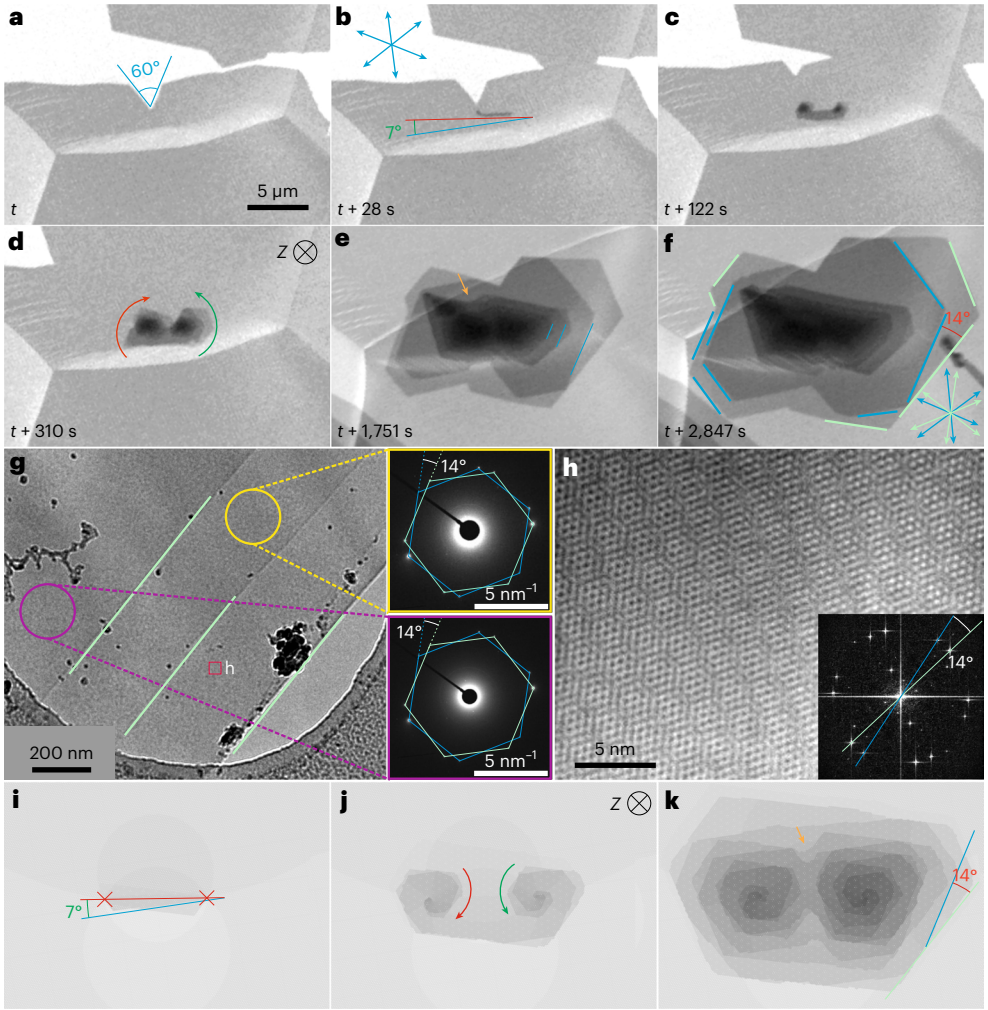

Fig. 3 | Growth and coalescence of GSs. a–**f**, In situ ESEM images of pairwise GS evolution with opposite screw dislocation handedness at different growing times, showing the chirality conversion from a 1D wrinkle to a twist angle of 3D stacking layers. The blue and light green lines and arrows indicate the zigzag-terminated edges and the corresponding growth direction, respectively. The wrinkle axis is along the red line in **b**. The scale bar in **a** also applies to **b**–**f**. **g**, TEM image of the GSs observed in **a**–**f** after coalescence inside the ESEM chamber, with the corresponding selected area electron diffraction patterns recorded from the regions highlighted by the yellow and purple circles. **h**, Atomically resolved image of stacked graphene layers (a magnification of the area highlighted by the red square in **g**) with the corresponding fast Fourier transform pattern shown in the inset. **i**–**k**, KMC simulations of the seamless coalescence of the GS pair (corresponding to **b**, **d** and **e**, respectively), where the nodal points in **i** are indicated by red crosses, and the red and green curved arrows in **j** denote the right- and left-handed spirals, respectively, where the arrow gives the direction of advance along the *z* axis.

Our KMC simulations (Fig. 3i–k) successfully reproduced the experimentally observed coalescence of the GSs and the moiré pattern (see Supplementary Fig. 4 and Supplementary Video 3), that is, the chiral angle of 7° and the twisting angle of 14°. The slightly different shape of the second layer between the experimental observation and the simulation was caused by the polygonal domain (Supplementary Fig. 5). This striking consistency between the experimental observation and theoretical modelling further validates our proposed mechanism of the 1D chirality to 2D twist-angle conversion.

It is important to note that multilayer graphene grown via the coalescence of GSs shows a clear layer-by-layer manner of growth (that is, Frank–van der Merwe growth) because the opposite Burgers vectors of the two spirals cancel each other out overall. Ignoring the central area of the multilayer graphene, where each GS appears, the stacking order of the multilayer graphene is exactly the same as that grown via layer-by-layer nucleation. This explains the broadly observed multilayer graphene growth in many CVD processes, where the multilayer region is generally very thick and the twist angles are well defined[22,33,34]. Moreover, the GSs synthesized here, which consist of an intertwined helical structure with a twist angle between odd/even layers, appear to be different from previous van-der-Waals-layered Eshelby-twist spirals[35,36].

Moreover, understanding how the twist angle can be controlled through the orientation of the initial wrinkle with respect to the zigzag direction of the basal graphene provides an approach towards the controlled growth of extended layer stacks with a defined twist angle. All that needs to be done is to seed the growth from a highly active oriented Pt grain onto a stepped vicinal grain that is oriented in a pre-defined way with respect to the zigzag orientation of the graphene that will initiate first on the most active grain. Grain-dependent catalytic activity and the spillover of graphene growth from the highly active grain to the grain with low activity is possible and has been achieved (Supplementary Video 4). Once the stepped grain is covered by a uniform overlayer, an annealing step, as described in this work, will result in the reconstruction of the stepped grain via expansion of the templating grain with high activity. During this process, wrinkles will form along

https://doi.org/10.1038/s41563-023-01632-y

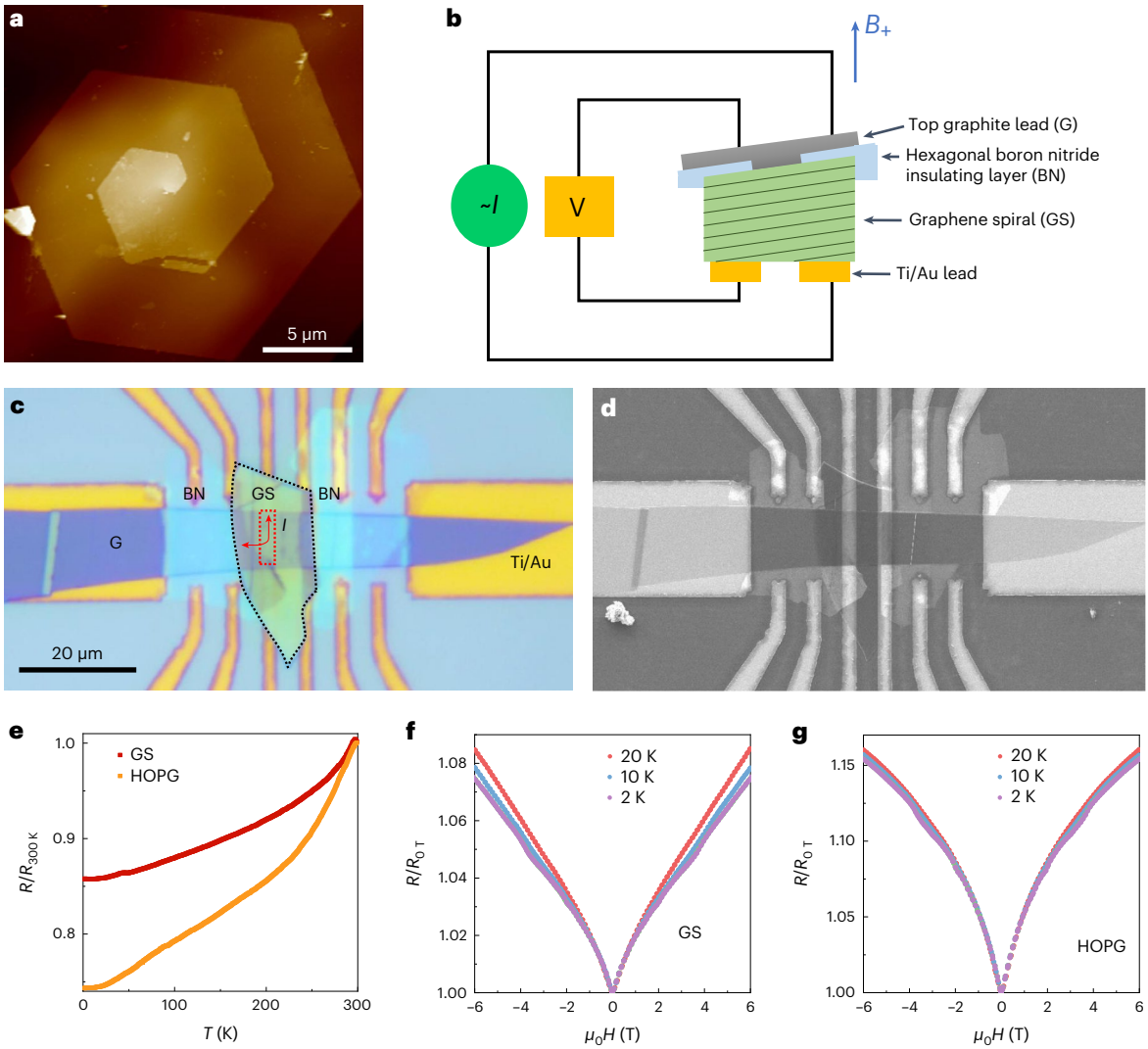

Fig. 4 | Comparison of transport properties between GS and HOPG. a, AFM image of a GS sample showing the exact centre of the GS. **b**, Schematic image illustrating the setup for measurement of the transport properties. Here, electrical current (*I*) flowing through the out-of-plane direction of the sample was recorded under a magnetic field (*B*) applied along the same direction. **c**,**d**, Optical (**c**) and ESEM (**d**) images showing a top view of the measurement setup. The scale bar in **c** also applies to **d**. **e**, Temperature dependence of the normalized resistance $R/R_{300\,K}$ for the GS (red) and HOPG (orange), where the GS sample always shows a larger vertical resistance. **f**,**g**, Normalized magnetoresistance $R/R_{0\,T}$ for the GS (**f**) and HOPG (**g**) samples at 2 K (violet), 10 K (blue) and 20 K (red).

the original step edges. Subsequently, wrinkle etching and re-growth can be applied. Although this work outlines the path and shows the possibility of the mechanism, some engineering and process optimization will be required to scale up the process.

Multilayer graphene growth initiated by multiple graphene spirals

The presented mechanism of GS formation can be tested against experimental results and used to reverse derive the structure of multilayer graphene. Extended Data Figure 9a shows a complex vertical stacking order that has previously been interpreted as 30°–30° rotation between successive layers[22]. Closer inspection illustrates that the stack consists of alternating polycrystalline and single-crystalline layers. The polycrystalline layers can be identified by the concave corners that are highlighted in Extended Data Fig. 9a by white arrows[37]. Identical shapes are regularly repeated, in one-layer intervals, with alternating odd- and even-numbered layers. The odd-numbered layer shows the intrinsic hexagonal shape of graphene, while the even-numbered layer appears to have a specific concave polygonal shape, as highlighted using the different coloured lines in Extended Data Fig. 9a. This oscillatory behaviour in the shapes of the even- and odd-numbered layers in multilayer graphene indicates that the odd/even layers have some connection and result in a similar shape. The strength of the graphene–substrate interaction is less influential on the layer growth in the out-of-plane direction, with a distinction between the even–odd layer number. Thus, the multilayer stacking structure is essentially due to the coalescence of GSs. The shape of the even–odd layer provides clues to reverse derive the orientation of the spirals and their initiation. As addressed in Extended Data Fig. 8v, the concave polygonal even layers imply a polycrystalline film, and are thus attributed to the coalescence of misaligned spirals with opposite handedness along the same glide plane[37], while the hexagonal odd layers result from the coalescence of aligned spirals with opposite handedness. Based on the shapes of the even–odd layers and the fundamental principle of screw dislocation initialization from graphene wrinkles (see Extended Data Fig. 8), the spiral orientation, rotation and the Burgers vector can be

estimated. Whereas the nodal-point layout, which contains five nodal points (spiral cores), as demonstrated in Extended Data Fig. 9b–d, is the minimal set of spirals required to reproduce the final shape of the spiral crystal shown in Extended Data Fig. 9c, additional spiral cores aligned in parallel to these five points do not change the final shape of the spiral crystal. To rationalize the reverse inference of the GS structure (Extended Data Fig. 9b,c), we simulated the shape evolution of GSs using conjectural nodal-point layout (see Extended Data Fig. 9d). The evolution of the GSs during growth was simulated using the KMC method, starting from a cracked and torn folded-over wrinkle (see Supplementary Fig. 6). The simulated coalescence shape of the GSs (Extended Data Fig. 9e–h) successfully recreated the experimentally observed shapes, providing further validation of the rationalities and efficiencies of the theoretical model.

Macroscopic crystals and properties

The real-time imaging results confirm that the spiral growth of graphene can be maintained under well-controlled CVD environments at 1,400 °C (Fig. 3a–f). This fabrication method offers the possibility to grow a large in-plane area GS for electrical-transport measurements. Indeed, using in situ observation-assisted CVD (see Methods), we achieved the growth of a large-area GS on a Pt surface (Extended Data Fig. 10 and Supplementary Fig. 7). Figure 4a shows an atomic force microscopy (AFM) image of the GS. To measure the transport properties along the spiral axis, we fabricated the setup presented in Fig. 4b. For reference, a highly ordered pyrolytic graphite (HOPG) sample with the same thickness was also measured. Figure 4e shows a plot of the *z*-axis normalized resistance values ($R/R_{300\,K}$) for both samples recorded from 300 to 2 K. The spiral exhibits a *z*-axis resistivity that is roughly two-thirds that of HOPG and shows semimetallic behaviour. We ascribe this difference to the presence of continuously rotating graphene layers in the GS sample. For Bernal-stacked (AB) or rhombohedral-stacked (ABC) graphite, the current flows directly across layers. For the GS, however, at least three channels, for example, along the spiral direction, across the layers and across the GS core, may carry current flow under an electric field applied parallel to the *z* axis. Since the in-plane mobility of carriers is orders of magnitude larger than that of the other two channels, it is most likely that primary current flow follows the in-plane spiral direction (Supplementary Fig. 8). For the magnetoresistance of the GS, linear behaviour is observed in the high-field region (Fig. 4f). This differs from that observed in HOPG (Fig. 4g). Moreover, for the intertwined GSs, the magnetoresistivity along the *z* axis could be twist-angle-dependent. To evaluate this quantitatively, we used a four-terminal measurement setup (Supplementary Fig. 9) in which the top graphene layer is separated into two leads, so that we can avoid contact resistance and obtain the resistivity more accurately. We observed fundamentally different *z*-axis resistivity and magnetoresistivity along the two resulting GSs. Supplementary Figure 10 shows the *z*-axis resistivity for a GS with a twist angle of ~7.4°. Negative magnetoresistivity is observed at low field, which could be due to weak localization that occurs as a result of the superlattice structure[38]. Supplementary Figure 11 shows similar measurements obtained for a GS sample with a twist angle of ~1.5°, which clearly show that the magnetoresistance is considerably different from the GS with the ~7.4° twist angle. Investigations into the twist-angle dependence of the magnetoresistivity could be a subject of future investigations.

Conclusion and outlook

In summary, here we report a graphene origami–kirigami approach (wrinkling, folding, tearing and cracking) that leads to the spiral growth of graphene multilayers with controlled stacking orders. The coalescence of the graphene layers that originate from neighbouring GSs gives rise to Frank–van der Merwe growth behaviour. This process converts the chirality of a 1D graphene wrinkle into the twist angles of 2D stacking layers of graphene. The kinetic pathways are observed via real-time imaging, and the abstracted mechanism for chirality conversion is validated through theory-based simulations of the spiral evolution. With such a fundamental understanding, the growth of intertwined GSs with fixed twist angles has been achieved. Thus, the twisted stacked graphene layers with misalignment between adjacent layers are tunable by varying the chiral graphene wrinkle, and are of interest due to their unconventional superconductivity[6]. In addition, this work has profound implications in the development of future nano-inductance devices and provides a step towards the scalable fabrication of multilayered graphene with defined twist angles. According to the mechanism reported in this work, by making use of the orientation-dependent catalytic properties of Pt, seeded growth and substrate engineering can be used for the tailored formation of layer stacks with pre-defined twist angles. In the future, using SPM as a tool in the electron microscopy setup, the mechanical manipulation of graphene can be tracked directly in real space with precise on-site correlation in real time[39]. With such a setup, the origami–kirigami processes can be accurately controlled via SPM tip manipulation during CVD conditions, and, accordingly, the pre-defined density of spiral nucleation sites and a designed twist angle can also be achieved.

Overall, this origami–kirigami approach results in 1D to 2D angle conversion and enables us to engineer the twisting angles in multilayered graphene, which is, in principle, applicable for all foldable 2D materials. Our study therefore offers a potential method to convert the chirality of 1D wrinkles into the twist angle of vertically stacked 3D superlattices.

Online content

Any methods, additional references, Nature Portfolio reporting summaries, source data, extended data, supplementary information, acknowledgements, peer review information; details of author contributions and competing interests; and statements of data and code availability are available at https://doi.org/10.1038/s41563-023-01632-y.

References

1. Xu, X. et al. Ultrafast epitaxial growth of metre-sized single-crystal graphene on industrial Cu foil. *Sci. Bull.* **62**, 1074–1080 (2017).
2. Wang, L. et al. Epitaxial growth of a 100-square-centimetre single-crystal hexagonal boron nitride monolayer on copper. *Nature* **570**, 91–95 (2019).
3. Trambly de Laissardière, G., Mayou, D. & Magaud, L. Localization of Dirac electrons in rotated graphene bilayers. *Nano Lett.* **10**, 804–808 (2010).
4. Suárez Morell, E., Correa, J. D., Vargas, P., Pacheco, M. & Barticevic, Z. Flat bands in slightly twisted bilayer graphene: tight-binding calculations. *Phys. Rev. B* **82**, 121407 (2010).
5. Kim, K. et al. Tunable moiré bands and strong correlations in small-twist-angle bilayer graphene. *Proc. Natl Acad. Sci. USA* **114**, 3364–3369 (2017).
6. Cao, Y. et al. Unconventional superconductivity in magic-angle graphene superlattices. *Nature* **556**, 43–50 (2018).
7. Hennig, G. R. Screw dislocations in graphite. *Science* **147**, 733–734 (1965).
8. Xu, F., Yu, H., Sadrzadeh, A. & Yakobson, B. I. Riemann surfaces of carbon as graphene nanosolenoids. *Nano Lett.* **16**, 34–39 (2016).
9. Patel, A. R. & Bahl, O. P. Evidence of screw dislocations in graphite. *Br. J. Appl. Phys.* **16**, 169–171 (1965).
10. Sun, Y. Q., Alemany, L. B., Billups, W. E., Lu, J. X. & Yakobson, B. I. Structural dislocations in anthracite. *J. Phys. Chem. Lett.* **2**, 2521–2524 (2011).
11. Allen, M. J. et al. Chemically induced folding of single and bilayer graphene. *Chem. Commun.* 6285–6287 (2009).
12. Mu, J. K. et al. Origami-inspired active graphene-based paper for programmable instant self-folding walking devices. *Sci. Adv.* **1**, e1500533 (2015).

13. Ebbesen, T. W. & Hiura, H. Graphene in 3-dimensions: towards graphite origami. *Adv. Mater.* **7**, 582–586 (1995).
14. Blees, M. K. et al. Graphene kirigami. *Nature* **524**, 204–207 (2015).
15. Miskin, M. Z. et al. Graphene-based bimorphs for micron-sized, autonomous origami machines. *Proc. Natl Acad. Sci. USA* **115**, 466–470 (2018).
16. Wang, Z.-J. et al. Direct observation of graphene growth and associated copper substrate dynamics by in situ scanning electron microscopy. *ACS Nano* **9**, 1506–1519 (2015).
17. Hillert, M. On the theory of normal and abnormal grain growth. *Acta Metall.* **13**, 227–238 (1965).
18. Wu, M. et al. Seeded growth of large single-crystal copper foils with high-index facets. *Nature* **581**, 406–410 (2020).
19. Jin, S. et al. Colossal grain growth yields single-crystal metal foils by contact-free annealing. *Science* **362**, 1021–1025 (2018).
20. Sutter, P. W., Flege, J.-I. & Sutter, E. A. Epitaxial graphene on ruthenium. *Nat. Mater.* **7**, 406–411 (2008).
21. Zhu, W. et al. Structure and electronic transport in graphene wrinkles. *Nano Lett.* **12**, 3431–3436 (2012).
22. Wang, Z.-J. et al. Stacking sequence and interlayer coupling in few-layer graphene revealed by in situ imaging. *Nat. Commun.* **7**, 13256 (2016).
23. Yang, R. et al. An anisotropic etching effect in the graphene basal plane. *Adv. Mater.* **22**, 4014–4019 (2010).
24. Chen, H. et al. Atomically precise, custom-design origami graphene nanostructures. *Science* **365**, 1036–1040 (2019).
25. Zhao, Y. et al. Supertwisted spirals of layered materials enabled by growth on non-Euclidean surfaces. *Science* **370**, 442–445 (2020).
26. Zhang, K. & Arroyo, M. Understanding and strain-engineering wrinkle networks in supported graphene through simulations. *J. Mech. Phys. Solids* **72**, 61–74 (2014).
27. Pereira, V. M., Castro Neto, A. H., Liang, H. Y. & Mahadevan, L. Geometry, mechanics, and electronics of singular structures and wrinkles in graphene. *Phys. Rev. Lett.* **105**, 156603 (2010).
28. Tay, R. Y. et al. Concentric and spiral few-layer graphene: growth driven by interfacial nucleation vs screw dislocation. *Chem. Mater.* **30**, 6858–6866 (2018).
29. Rakovan, J. & Jaszczak, J. A. Multiple length scale growth spirals on metamorphic graphite {001} surfaces studied by atomic force microscopy. *Am. Mineral.* **87**, 17–24 (2002).
30. Frank, F. C. & Read, W. T. Multiplication processes for slow moving dislocations. *Phys. Rev.* **79**, 722–723 (1950).
31. Wang, Z. J. et al. The coalescence behavior of two-dimensional materials revealed by multiscale in situ imaging during chemical vapor deposition growth. *ACS Nano* **14**, 1902–1918 (2020).
32. Nabarro, F. R. N. The force between two screw dislocations. *Philos. Mag. A* **54**, 577–582 (1986).
33. Karamat, S. et al. Coalescence of few layer graphene grains grown by chemical vapor deposition and their stacking sequence. *J. Mater. Res.* **31**, 46–54 (2016).
34. Sun, J. et al. Growth mechanism of graphene on platinum: surface catalysis and carbon segregation. *Appl. Phys. Lett.* **104**, 152107 (2014).
35. Liu, Y. et al. Helical van der Waals crystals with discretized Eshelby twist. *Nature* **570**, 358–362 (2019).
36. Sutter, P., Wimer, S. & Sutter, E. Chiral twisted van der Waals nanowires. *Nature* **570**, 354–357 (2019).
37. Guo, W. et al. Governing rule for dynamic formation of grain boundaries in grown graphene. *ACS Nano* **9**, 5792–5798 (2015).
38. Niyogi, S. et al. Covalent chemistry for graphene electronics. *J. Phys. Chem. Lett.* **2**, 2487–2498 (2011).
39. Schweizer, P. et al. Mechanical cleaning of graphene using in situ electron microscopy. *Nat. Commun.* **11**, 1743 (2020).

[1]School of Physical Science and Technology, ShanghaiTech University, Shanghai, China. [2]School of Natural Sciences, Technical University Munich, Munich, Germany. [3]Center for Transformative Science, ShanghaiTech University, Shanghai, China. [4]Institute of Technology for Carbon Neutrality, Shenzhen Institute of Advanced Technology, Chinese Academy of Sciences, Shenzhen, China. [5]Shanghai Institute of Microsystem and Information Technology, Chinese Academy of Sciences, Shanghai, China. [6]Institute of Physics, Chinese Academy of Sciences, Beijing, China. [7]Advanced Research Institute of Multidisciplinary Science, Beijing Institute of Technology, Beijing, China. [8]ShanghaiTech Laboratory for Topological Physics, ShanghaiTech University, Shanghai, China. [9]Beijing Key Laboratory of Optoelectronic Functional Materials & Micro-Nano Devices, Department of Physics, Renmin University of China, Beijing, China. [10]Institute of Physical Engineering, Faculty of Mechanical Engineering, Brno University of Technology, Brno, Czech Republic. [11]Central European Institute of Technology (CEITEC), Brno University of Technology, Brno, Czech Republic. [12]Department of Physics, University of Oxford, Oxford, UK. [13]State Key Laboratory of Low Dimensional Quantum Physics and Department of Physics, Tsinghua University, Beijing, China. [14]Beijing Key Laboratory of Green Chemical Reaction Engineering and Technology, Department of Chemical Engineering, Tsinghua University, Beijing, China. [15]Vacuum Interconnected Nanotech Workstation, Suzhou Institute of Nano-Tech and Nano-Bionics, Chinese Academy of Sciences, Suzhou, China. [16]State Key Laboratory for Mesoscopic Physics, Frontiers Science Center for Nano-optoelectronics, School of Physics, Peking University, Beijing, China. [17]International Center for Quantum Materials, Collaborative Innovation Center of Quantum Matter, Peking University, Beijing, China. [18]State Key Laboratory of Catalysis, Dalian Institute of Chemical Physics, Chinese Academy of Sciences, Dalian, China. [19]School of Physical Sciences, University of the Chinese Academy of Sciences, Beijing, China. [20]CAS Center for Excellence in Topological Quantum Computation, University of the Chinese Academy of Sciences, Beijing, China. [21]These authors contributed equally: Zhu-Jun Wang, Xiao Kong, Yuan Huang, Jun Li. ✉e-mail: wangzhj3@shanghaitech.edu.cn; wji@ruc.edu.cn; f.ding@siat.ac.cn; marc.willinger@tum.de

Methods

In situ ESEM observations

In situ CVD growth experiments were performed inside the chamber of a modified commercial ESEM (Quattro ESEM, Thermo Fisher). The vacuum system of the ESEM was modified and upgraded with oil-free pre-vacuum pumps. The instrument is equipped with a home-made laser heating stage, a gas supply unit (using mass flow controllers from Bronkhorst) and a mass spectrometer (OmniStar, Pfeiffer) for analysis of the chamber atmosphere. Owing to the use of rubber O-rings for sealing and the fact that the chamber cannot be baked out, the base pressure of the instrument is around 2×10^{-5} Pa, with a residual gas composition comprising mostly water, N_2 and O_2. After each sample loading, the chamber was pumped out to around 10^{-3} Pa, purged with pure N_2, and pumped again to 10^{-3} Pa successively several times. Under the CVD growth conditions, the pressure is six orders of magnitude higher than the base pressure and is made up mostly of H_2 (99.9995% purity) and C_2H_4 (99.95% purity). Samples of sizes ranging from 4 × 4 mm to 5 × 5 mm are extracted from a 0.2-mm-thick Pt foil (99.999% purity). Before all CVD growth experiments, the chamber of the ESEM was plasma cleaned. The Pt foil was annealed at 1,000 °C under a H_2 flow of 10 sccm at 25 Pa for more than 48 h inside the chamber. The temperature was measured using a type B thermocouple that was spot-welded onto the substrate, which simultaneously served to ground the sample. CVD growth was performed at temperatures ranging from 1,000 °C to 1,400 °C, with a pressure in the chamber ranging from 25 Pa to 200 Pa. During the experiments, the microscope was operated at an acceleration voltage of 3.0–7.5 kV. Images were recorded using a large-field detector during the CVD growth conditions. No influence of the electron beam on the growth and etching process could be observed. The imaged regions and their respective surroundings showed similar behaviour, as demonstrated by changing the magnification or by moving the sample under the beam. Furthermore, no electron-beam-induced contamination was observed at elevated temperatures. To obtain graphene of superior quality for subsequent origami–kirigami processes, we subjected the as-grown graphene to annealing under the appropriate conditions for CVD growth. This annealing process served to repair defects and adjust the positioning of grain boundaries in the graphene[40–42].

In situ observation-assisted CVD growth

To fabricate large-area GS samples, CVD growth needs to be carried out above 1,400 °C to maintain the Frank–van der Merwe growth. The home-made cold-wall laser CVD chamber is attached to the in situ ESEM and shares an identical atmosphere. During CVD growth, the temperature is the same as in the in situ ESEM setup. In this way, the surface dynamic process can be assessed accurately via in situ ESEM observation. The CVD chamber incorporates a plasma generator that can conduct plasma-enhanced assisted CVD growth. In addition, we image the grain growth of the Pt substrate directly after the surface is fully covered by graphene. The growth atmosphere and relevant parameters can be manipulated directly and tuned based on feedback from the in situ observations. This real-time imaging assistance enables us to achieve better control over spiral formation and avoid less favourable outcomes.

Frank–van der Merwe (layer-by-layer) growth can be sustained at elevated temperatures. Supplementary Figure 12 shows a GS after growth for one hour in an ESEM chamber at 1,400 °C. The sample was prepared using a site-specific focused ion beam (FIB) lift-out technique. A cross-sectional scanning transmission electron microscopy (STEM) image (Supplementary Fig. 12b) reveals that the number of layers is approximately 28. It is possible to maintain Frank–van der Merwe growth in thicker GS samples by increasing the growth temperature and/or extending the growth time. The FIB preparation of a GS sample, grown at a higher temperature and for a longer time (around 1,450 °C for 1.5 h), is depicted in Supplementary Fig. 12c. The cross-sectional STEM image (Supplementary Fig. 12d) shows that it is thicker, with approximately 40 layers. These results indicate that the number of layers can be controlled using pre-calibrated growth conditions, and GS samples of tens of layers can be obtained in a reasonable growth time (~1 h) and at an accessible temperature (over 1,400 °C).

Electron backscatter diffraction

Electron backscatter diffraction (EBSD) patterns were acquired using a DigiView detector (EDAX) installed on a FEI Nova NanoSEM 230 microscope. Analysis of the EBSD patterns, including phase identification and the generation of orientation maps, was carried out using the OIM 5.31 program (EDAX).

Scanning tunnelling microscopy

STM measurements were carried out at room temperature using an ultrahigh vacuum system with a base pressure in the region of 10^{-8} Pa, equipped with STM and low-energy electron diffraction apparatus, an argon-ion sputtering gun, a laser heating stage and a gas feeding system. The images were recorded with a constant current mode using a home-made tungsten tip.

Transmission electron microscopy

TEM experiments were carried out using an aberration-corrected Titan Themis G2 300 system (FEI) operated with an aberration-corrected Grand ARM300 instrument (JEOL) at 80 kV. The electron beam dose rate was minimized to 10^4 electrons per Å^2 per s to minimize the knock-on damage for graphene. For high-resolution TEM imaging, the spherical aberration was corrected to around −5 µm. The two-fold astigmatism was corrected to ~0 nm. The coma and three-fold astigmatism were corrected to several nanometres.

Quantitative TEM/STEM simulations

The widely used open-source program was applied to carry out quantitative TEM/STEM simulations (QSTEM)[43–45]. For TEM image simulations (Supplementary Fig. 4), the multi-slice method is applied to calculate the wave transfer function of the slices during QSTEM. The detailed parameters for QSTEM are: high voltage, 80 kV; defocus, −5.0 nm; Cs (spherical aberration) 0.0015 mm; focal spread, 5 nm.

Cross-sectional sample preparation

The cross-sectional GS samples were prepared using a multibeam FIB system (JIB-4700F, JEOL). To minimize ion-beam-induced damage, the whole FIB polishing process was carried out at a reduced voltage and ion-beam current. The GS was transferred directly onto the Au TEM grid. Then the sample was extracted using an accelerating voltage of 30 kV and a reduced ion beam of less than 1 nA. After the lamella had been transferred to an FIB lift-out grid, it was gradually thinned to approximately 200 nm using an ion beam with an accelerating voltage of 10 kV and gradually reducing the current of 100 pA to 30 pA. After that, the voltage was reduced further to 5 kV and a current as small as 10 pA was used for the final milling.

Atomic force microscopy

AFM images were recorded using a sharp nitride lever probe (SNL-10, Bruker). Imaging was carried out in tapping mode using a V-shaped cantilever probe B (a silicon tip on the nitride lever with a frequency f_0 = 40–75 kHz and a spring constant k = 0.32 Nm).

Transport measurements

Hall-bar electrodes on Si/SiO_2 substrates were fabricated using a standard photolithography technique, followed by the electron-beam evaporation of the Ti/Au (5/60 nm) electrodes. The GS was transferred onto the electrodes in a glovebox, and covered with hexagonal boron nitride for insulation, and then graphite was loaded onto the GS as

a top lead. Thus, the current can flow through the *z* axis of the GS, and the exact *z*-axis resistance can also be observed, as illustrated in Fig. 4b and Supplementary Fig. 8. Transport measurements were carried out using a physical property measurement system (PPMS, Quantum Design) cryostat. A constant alternating current of 1 μA above 10 Hz was applied for all the magnetotransport measurements. In order to compare the transport measurements along the *z* axis with various interlayer twist angles, the following protocols must be obeyed during the preparation of each sample device: (1) transfer the GS samples with different twisting angles from a Pt substrate with a similar area and thickness; (2) examine the sides of the GS samples carefully using an electron microscope to achieve precise transport measurements along the *z* axis; (3) clean the edges of the GS samples at the nanometre scale using a probe to prevent containment-induced out-of-plane short-cuts; and (4) transfer a GS sample that is identical to the one used in device measurements onto a TEM grid for TEM diffraction measurements for confirming the twist angle of the GS accurately, as illustrated in Supplementary Fig. 10 and Supplementary Fig. 11.

Data availability

Source data are provided with this paper. All other data that support the findings of this study are available within the Article and the Supplementary Information.

References

40. Rogge, P. C. et al. Real-time observation of epitaxial graphene domain reorientation. *Nat. Commun.* **6**, 6880 (2015).
41. Tyurnina, A. V., Okuno, H., Pochet, P. & Dijon, J. CVD graphene recrystallization as a new route to tune graphene structure and properties. *Carbon* **102**, 499–505 (2016).
42. Wang, Z. J. et al. Formation mechanism, growth kinetics, and stability limits of graphene adlayers in metal-catalyzed CVD growth. *Adv. Mater. Interfaces* **5**, 1800255 (2018).
43. Zhu, Y. et al. Unravelling surface and interfacial structures of a metal–organic framework by transmission electron microscopy. *Nat. Mater.* **16**, 532–536 (2017).
44. Pirart, J. et al. Reversed size-dependent stabilization of ordered nanophases. *Nat. Commun.* **10**, 1982 (2019).
45. Duerrschnabel, M. et al. Atomic structure and domain wall pinning in samarium-cobalt-based permanent magnets. *Nat. Commun.* **8**, 54 (2017).

Acknowledgements

This work was mainly supported by the National Natural Science Foundation of China under grant no. 12027804. We acknowledge the Center for High-Resolution Electron Microscopy of ShanghaiTech University for use of the electron microscope. W.J. thanks the National Natural Science Foundation (grant no. 11974422) and the Strategic Priority Research Program of the Chinese Academy of Sciences (grant no. XDB30000000). Y. Huang thanks the National Key Research and Development Program of China (grant no. 2019YFA0308000). H.-J.G. thanks the National Key Research & Development Projects of China (grant no. 2022YFA1204100) and the National Natural Science Foundation of China (grant no. 61888102). L.B. and H.Y. thank the Strategic Priority Research Program of the Chinese Academy of Sciences (XDB30000000) and the National Key Research & Development Projects of China (grant no. 2022YFA1204100). H.C. thanks the National Natural Science Foundation of China (grant no. 52022105).

Author contributions

Z.-J.W. conceived this project and supervised the research. Z.-J.W. modified the ESEM, planned and conducted the in situ growth experiments and did most of the ESEM data analysis. Z.-J.W., K.C., Y. Huang, P.B., M.K., Y. Hu, J.C., Z.C. and L.W. performed the TEM and AFM measurements. Theoretical simulations and implementation of the obtained results were carried out by X.K., K.L, W.J., Q.Z. and F.D. STM measurements were performed by Y. Cui, H.C., Zhongkai Liu, Zhi Liu, Y. Chen, H.-J.G. and X.B. Transport measurements were performed by L.B., Y.W., Y.Z., F.P., H.Y. and J.L. Important contributions to the interpretation of the results, conception and writing of the manuscript were made by Z.-J.W., F.D. and M.-G.W. All authors participated in the scientific discussion.

Competing interests

The authors declare no competing interests.

Additional information

Extended data is available for this paper at https://doi.org/10.1038/s41563-023-01632-y.

Supplementary information The online version contains supplementary material available at https://doi.org/10.1038/s41563-023-01632-y.

Correspondence and requests for materials should be addressed to Zhu-Jun Wang, Wei Ji, Feng Ding or Marc-Georg Willinger.

Peer review information *Nature Materials* thanks Peter Ercius and the other, anonymous, reviewer(s) for their contribution to the peer review of this work.

https://doi.org/10.1038/s41563-023-01632-y

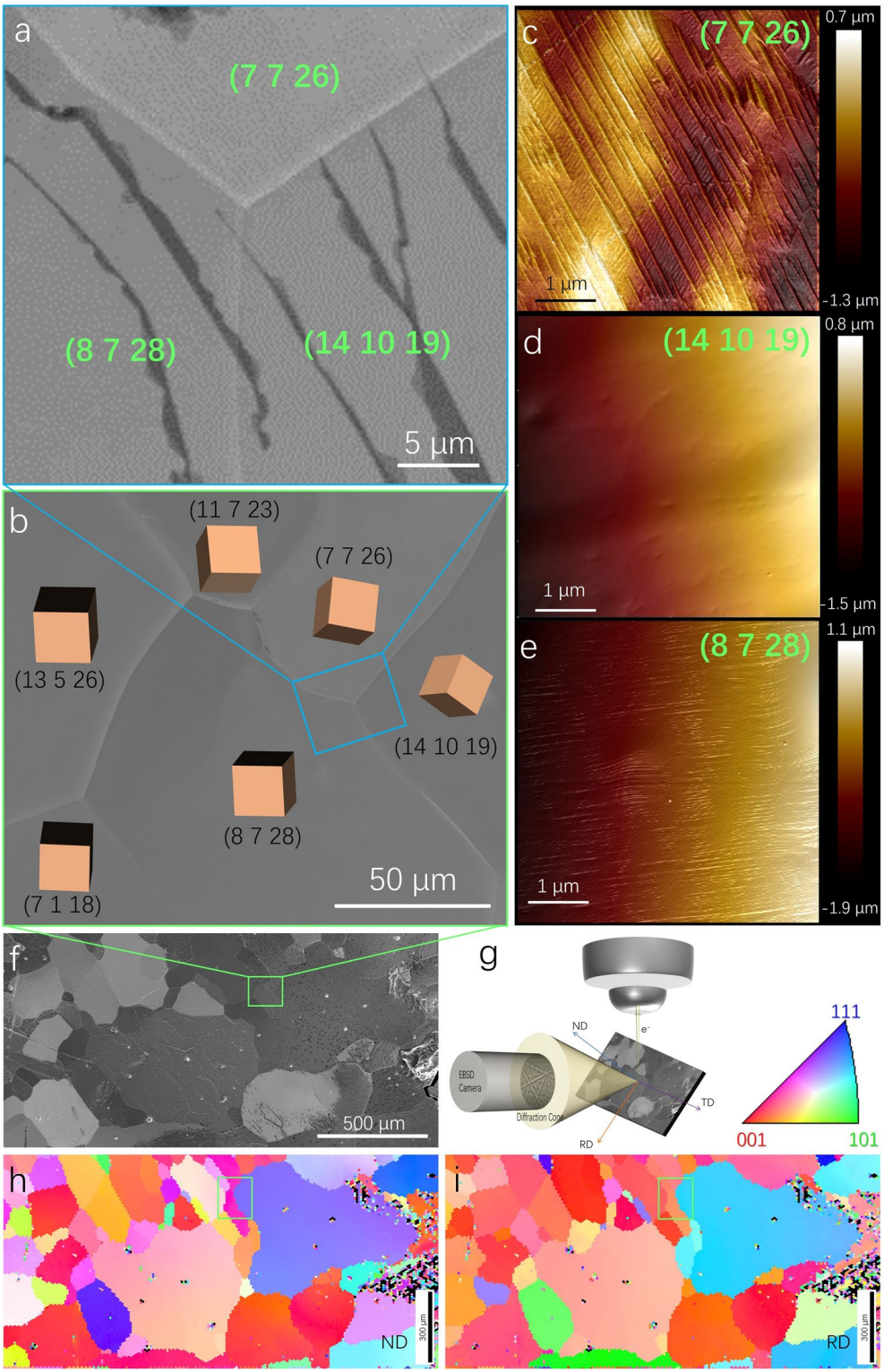

Extended Data Fig. 1 | Graphene-induced a variety of surface reconstruction on different Pt grain. (**a**) In situ ESEM images recorded the folded-over graphene wrinkle on Pt polycrystal surface at 1400 °C, 25 Pa. (**b**) Zoom-out SEM image showing wide-angle view of Pt substrate. (**c**–**e**) AFM images recorded from the same Pt grains imaged in (a). The graphene covered surfaces are characterized by graphene-induced Pt step bunching and surface reconstructions. (**f**) Global SEM image showing the overview morphology of Pt substrate. (**g**) Schematic of typical EBSD data collection showing the orientation of the crystal reference frame, from rolling (RD), transverse (TD) and normal (ND) orthogonal directions. The EBSD map recorded from a region in (**f**) is shown in (**h**) from ND, and in (**i**) from RD respectively. The different orientations of the cubic model represent the local orientation of Pt surface gains.

https://doi.org/10.1038/s41563-023-01632-y

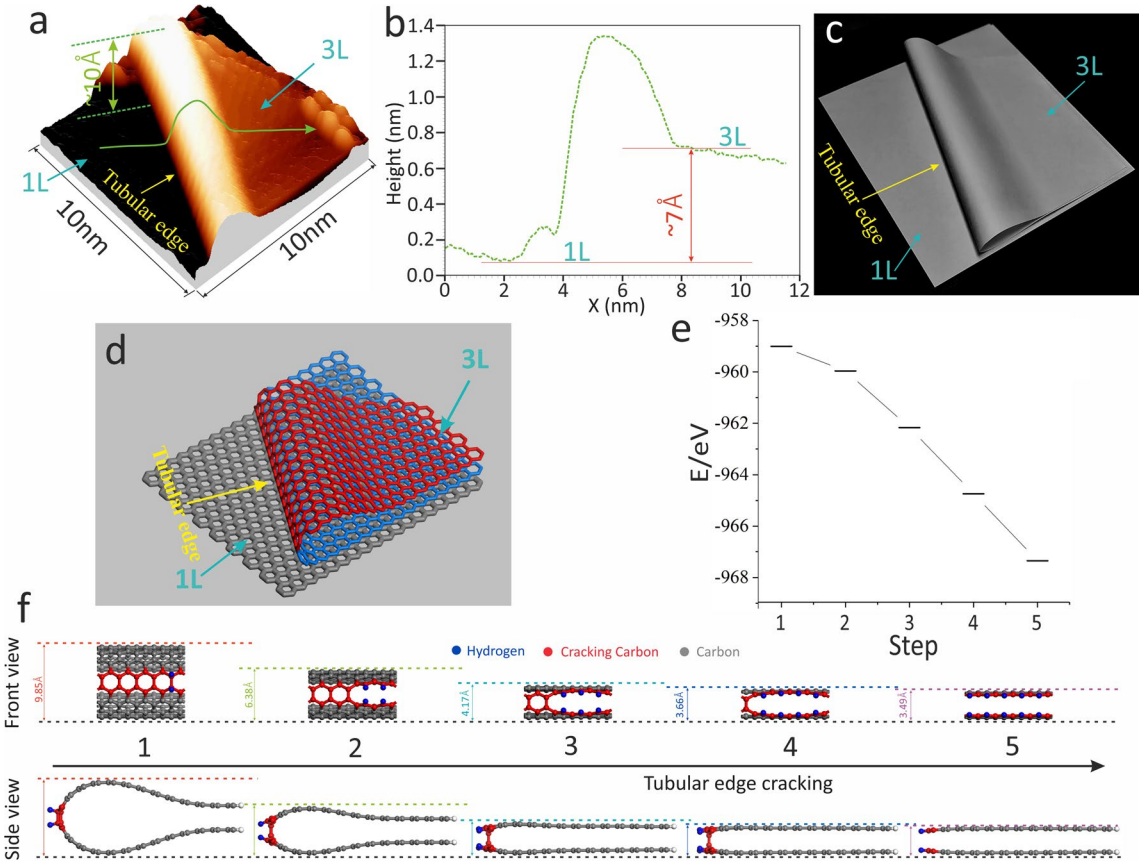

Extended Data Fig. 2 | Tubular edge structure. (**a**) Atomically resolved the curvature of tubular edge. (**b**) The height profile of the green line in (**a**). (**c**) Analogy with paper model for demonstration folded-over graphene wrinkle. (**d**) Schematic view showing folded-over graphene wrinkle. The cracking tubular edge energy profile as a function of the number of carbon atoms cracking is shown in (**e**). (**f**) The corresponding atomistic models used to calculate energies of the tubular edge cracking along zigzag direction (for details of the calculation, refer to the Methods section). Note: The DFT calculations were carried out to model the graphene cracking step on the basis of experimentally obtained values for the curvature of the tubular edge (**a**, **b**). (**f**) shows the modelled hydrogen etching process, in which an H2 molecule was attached at the point of the highest curvature; this attachment ultimately results in graphene cracking. The total energies of representative steps in the etching process (**e**) indicates the cracking is energetically favourable and further verifies the proposed graphene cracking mechanism.

https://doi.org/10.1038/s41563-023-01632-y

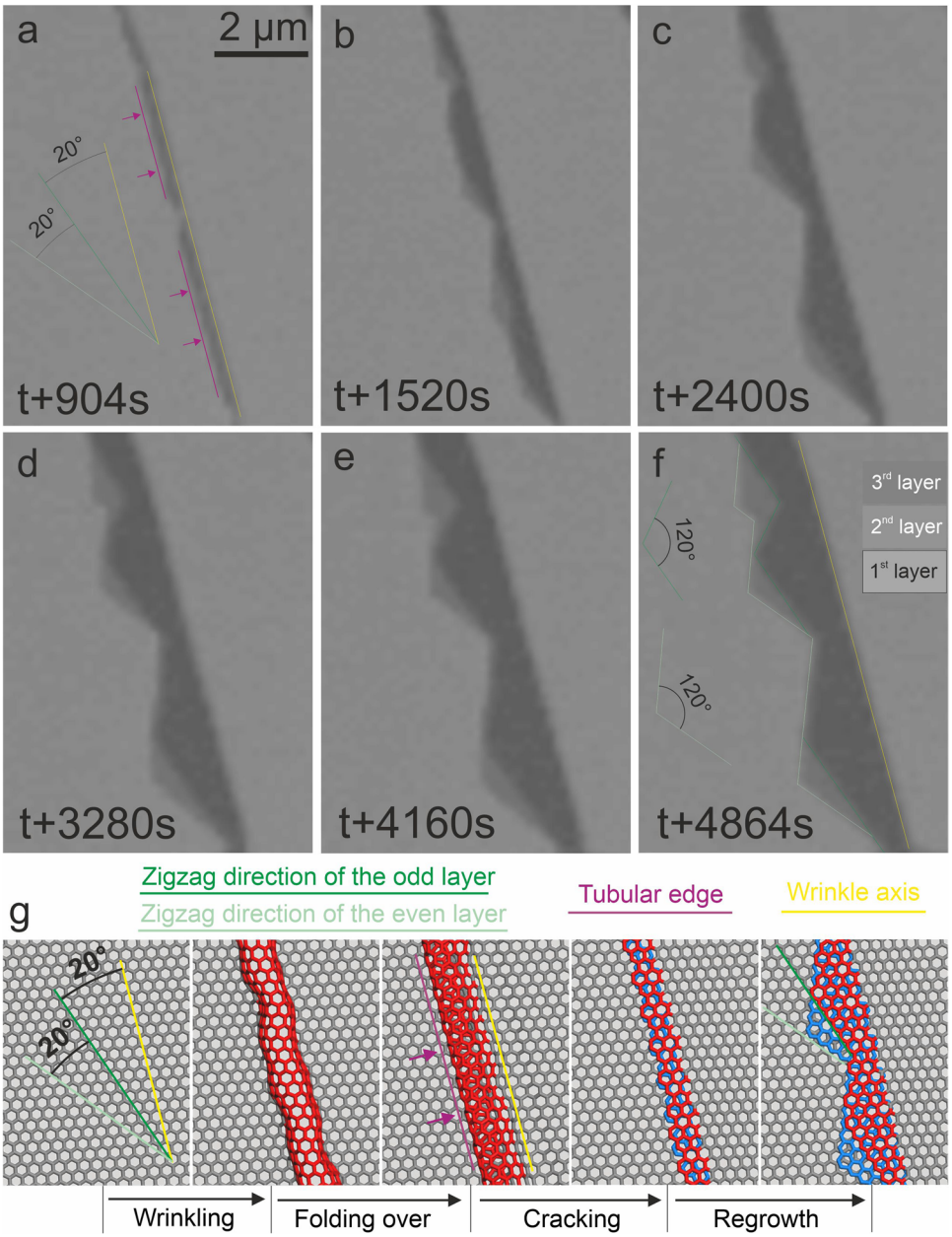

Extended Data Fig. 3 | Magnified region of yellow square in main text Fig. 1d in situ showing the formation of sawtooth graphene edges. (**a**) The folded-over graphene wrinkle. The purple lines highlight the tubular edges of folding-over wrinkle. (**b**–**f**) shape evolution of the etching along the tubular edge creates two new growth fronts that will relatively fast re-establish the typical zigzag growth fronts. This will lead to the formation of sawtooth graphene edges unless the crack in the tubular edge is parallel to a zigzag edge. As shown in (**f**) the second layer and the third layer is finally terminated by zigzag edges with 120° corner. The corresponding formation steps (graphene wrinkling, folding over, cracking and regrowth) are demonstrated in the schematics of (**g**) using origami-like paper folding. Green and light-green lines highlight the zigzag direction of the odd and even layer, respectively. Yellow line indicates wrinkle axis of wrinkle.

https://doi.org/10.1038/s41563-023-01632-y

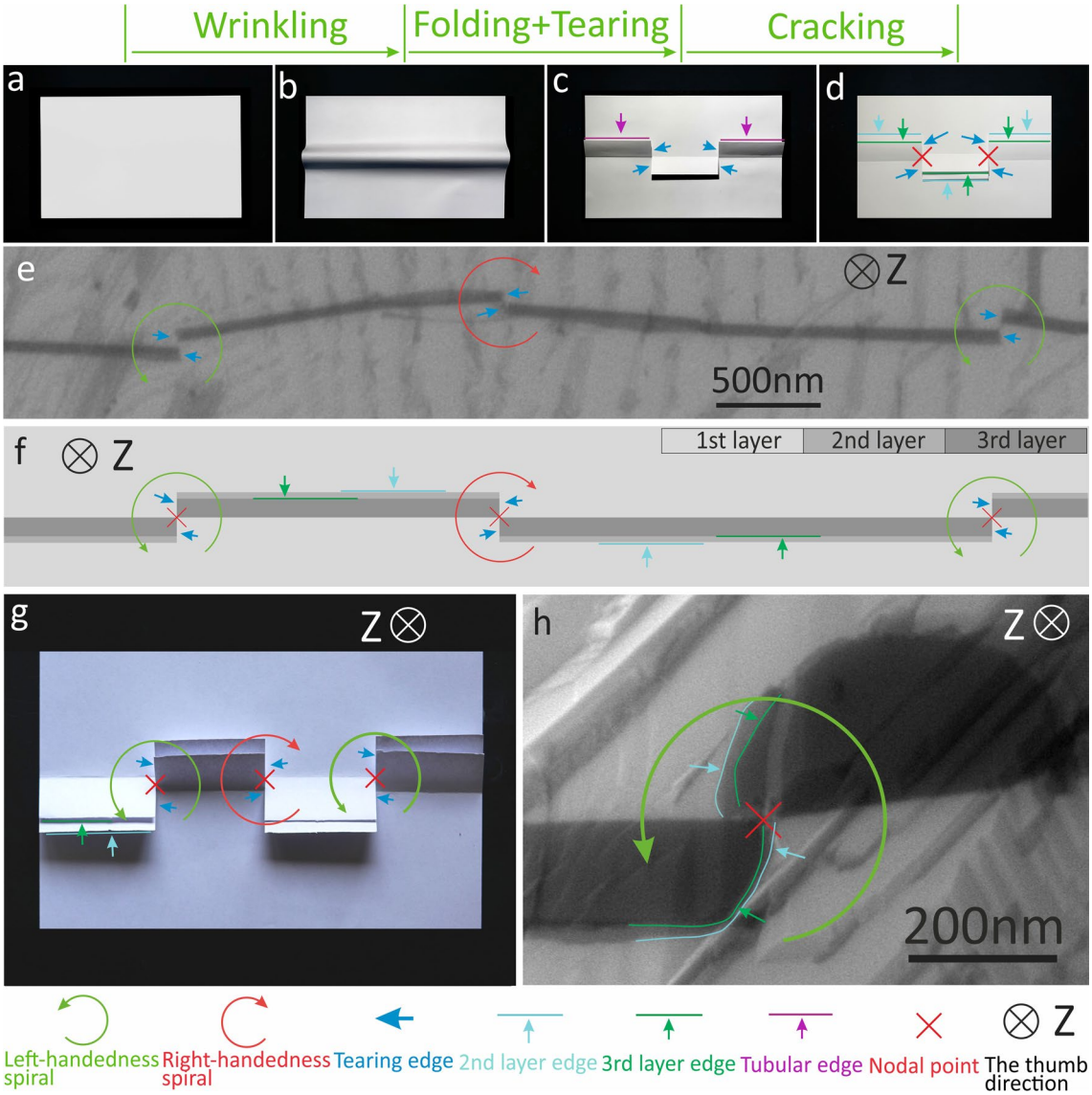

Extended Data Fig. 4 | Opposite handedness of the adjacent graphene spiral and Burger vector of screw core. (**a**–**d**) The analogy with paper model with two tearing nodal points (red crosses in **d**) was used to represent graphene origami-kirigami quadruplet (graphene wrinkling, folding, tearing and cracking). The folded wrinkles are easily detected in the ESEM imaging as elongated features of lower brightness, as shown in **e** (with a grey-level corresponding to 3-layer graphene), each of which contains one exposed layer edge (marked by green lines and arrows) and one buried layer edge (highlighted by light green lines and arrows). (**f**) Corresponding schematic view representing the contrast variation of SEM observation. (**g**), Origami-kirigami paper model representing the handedness of GSs at the nodal points of folding of collapsed wrinkle in (**e**). Note: The handedness of the resulting screw dislocation is defined by the sequence in which the wrinkle parts fold-over to the left or right along folding-axis. The tearing edges at a tearing point always have, as a consequence of the oppositely origami folding of wrinkles, reversed handedness to those at the two nearest adjacent tearing points, as marked by red and green curved arrows in (**e**–**h**). In situ ESEM images (**h**) recorded at 1400 °C, 25 Pa showing the two pair of tearing edges initializing the growth of two intertwined double spirals at the nodal point.

https://doi.org/10.1038/s41563-023-01632-y

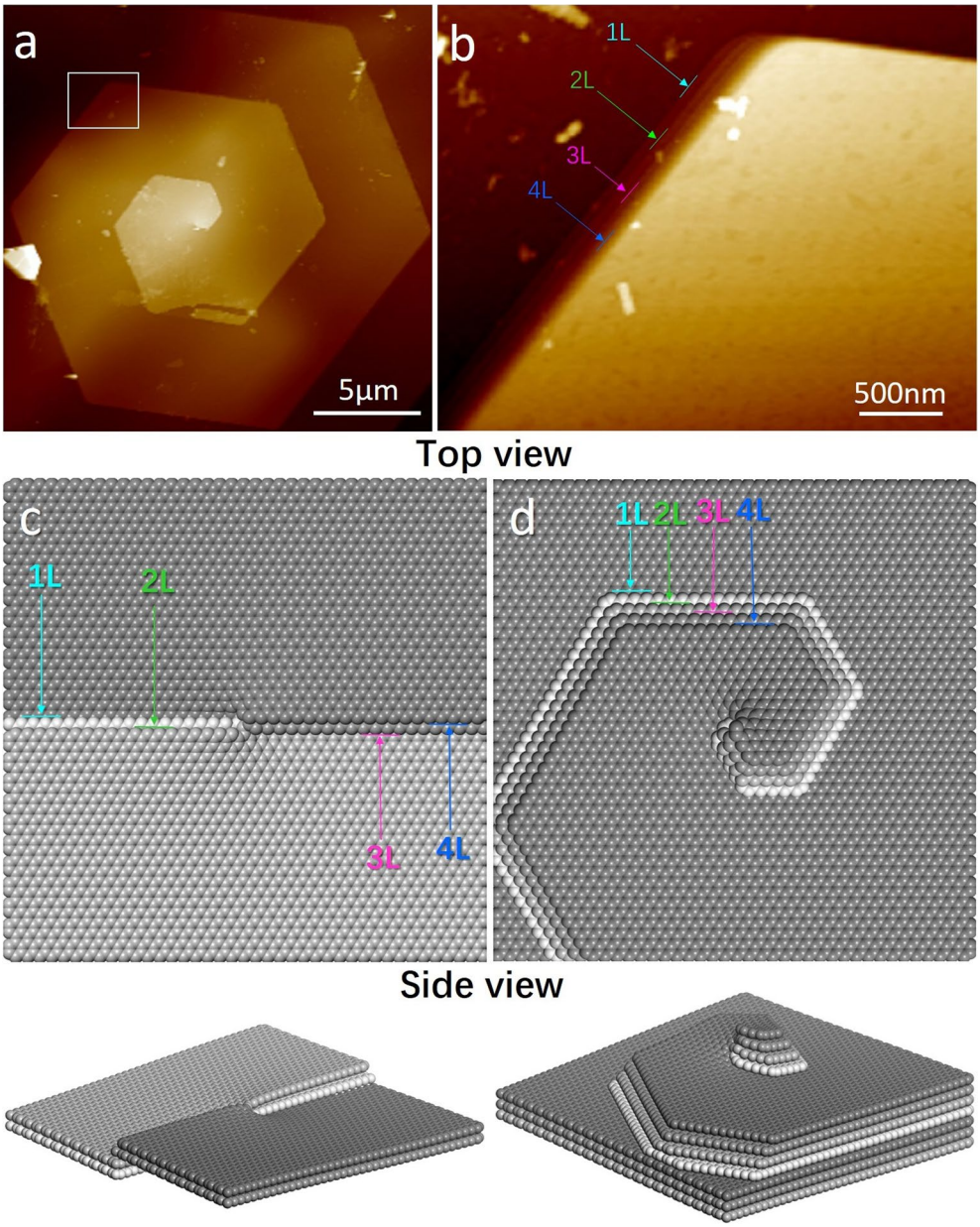

Extended Data Fig. 5 | Graphene spiral structure. (**a**) Atomic force microscopy imaging of GS structures. (**b**) The zoom-in of topography over the region indicated by the white square in (**a**) showing four intertwined spirals structure. (**c**,**d**) Schematic representation of initial state and final structure of graphene spiral in (**a**). Note: as-grown GS is fabricated by in situ observation assisted CVD method (see Methods in main text).

https://doi.org/10.1038/s41563-023-01632-y

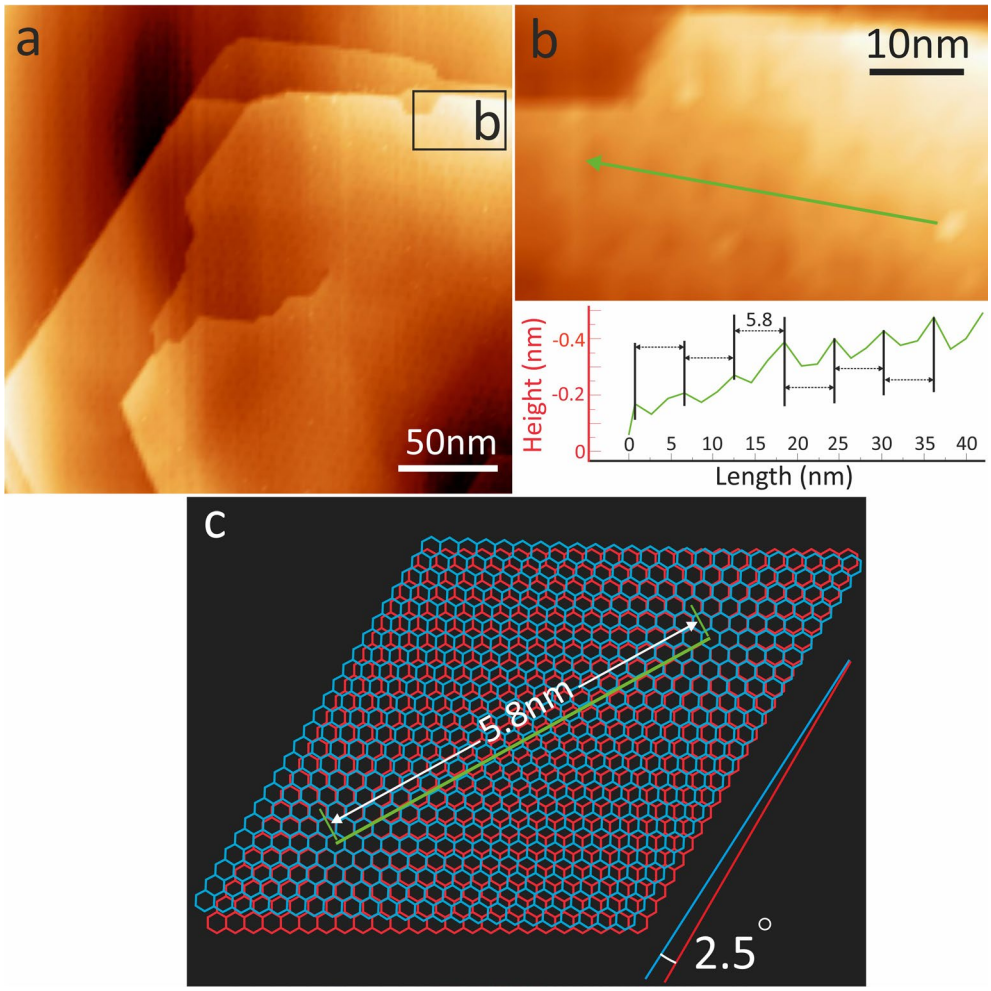

Extended Data Fig. 6 | Scanning tunnelling microscopy (STM) imaging of GS structures. The screw dislocation cores are seen in the STM images (**a**), and (**b**) is a zoom-in of local topography over the region indicated by the black window in panel (**a**). Height profile along the green line in (**b**) showing the Moiré corrugation. (**c**) The corresponding atomistic models used to reduce twist angle of top and bottom layers.

https://doi.org/10.1038/s41563-023-01632-y

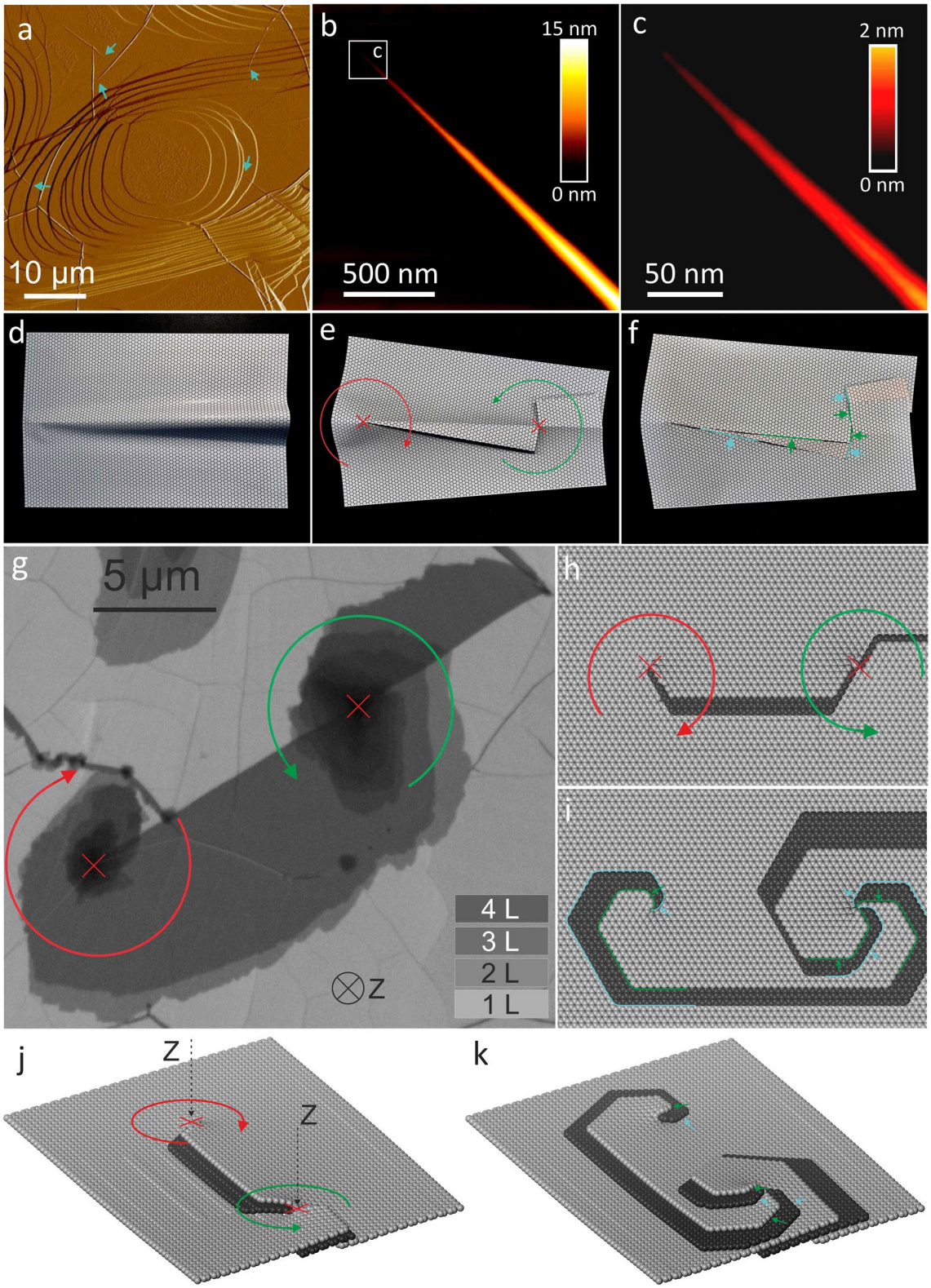

Extended Data Fig. 7 | Triggering spiral growth at the endpoints of wrinkle. (**a**) Large-area AFM image of CVD grown graphene on Pt substrate showing topography of graphene wrinkles. The apices of wrinkles are marked by light blue arrows. (**b**) The details of a tail end of wrinkle represent half cone shape, and (**c**) is a zoom-in of local topography over the region indicated by the white box in panel (**b**). (**d**–**f**) Analogy with paper model for demonstration the cracking of the tubular edge up to the apex of a wrinkle. (**g**) In situ ESEM images of GSs at 1400 °C showing the GSs morphology at the endpoints of wrinkle and at the middle of wrinkle. The corresponding schematic representation of the formation of GSs at the endpoints of wrinkle and at the middle of wrinkle in in-plane view (**h**,**i**) and out-of-plane view (**j**,**k**). Note: The two growth fronts formed at the endpoint of cracked tubular edge initialize two spirals growth. The handedness is indicated by the red (right-handedness) and green (left-handedness) curved arrows (the thumb giving the direction of advance along the Z-axis). The tearing nodal points (screw dislocation cores) are highlighted by red ×. The light blue and green arrows in (**f**,**i**,**k**) highlight growth front of GSs at nodal points.

https://doi.org/10.1038/s41563-023-01632-y

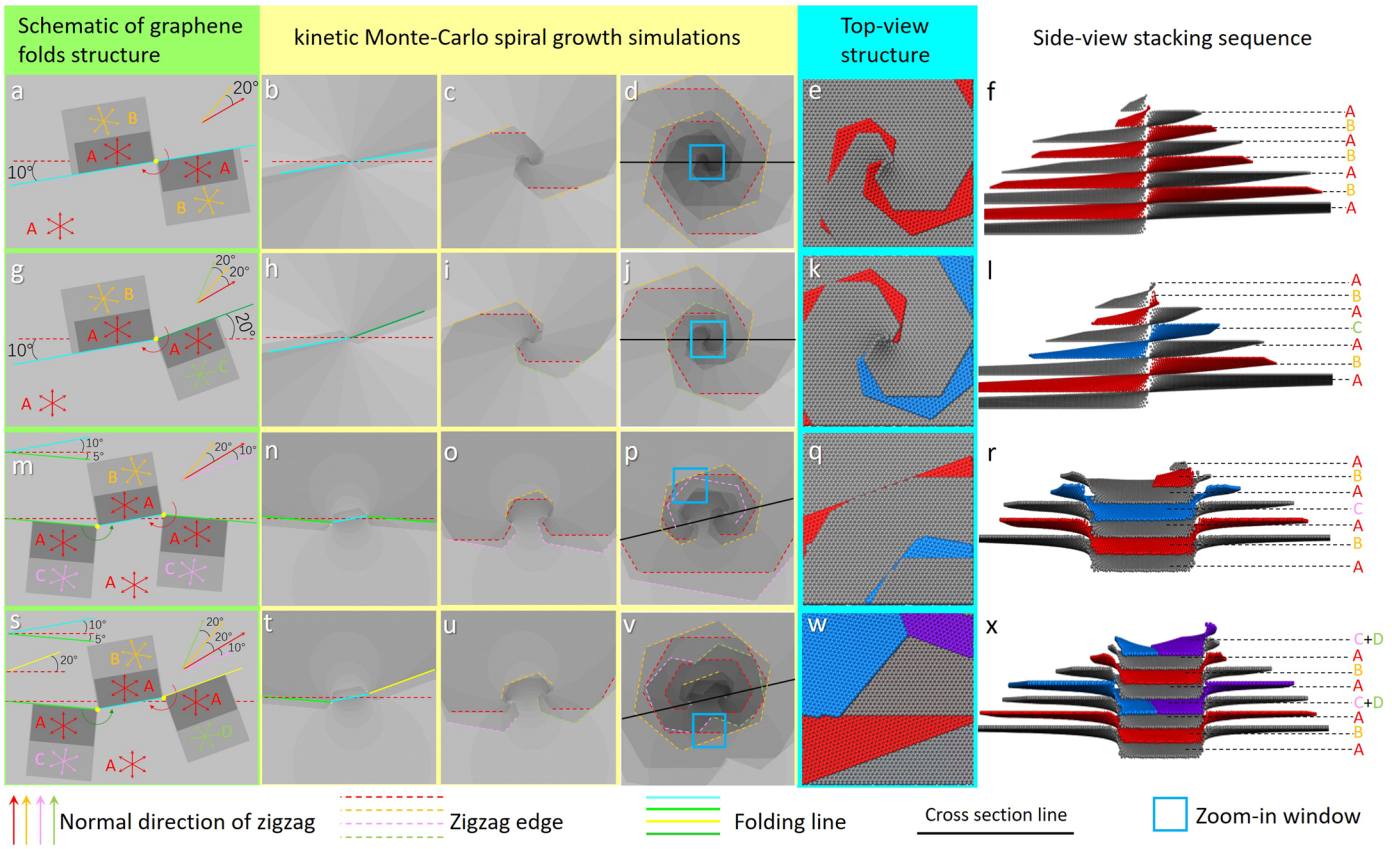

Extended Data Fig. 8 | Classifying the shape of twisted few-layer graphene by the orientations of fold-over wrinkles. (**a**) Schematic of the case which has two segments of cracked wrinkle with (10°, 10°) orientation to zigzag direction of basal layer, the radial arrows indicate normal direction of zigzag edge in each layer. The layers with same orientation are labelled by same alphabet (A, B, ...). (**b**–**d**) the snapshots in growth simulation of graphene corresponding to schematic (**a**). (**e**,**f**) Top view and side view of the final structure corresponding to schematic (**a**). (**g**) Schematic of the case which has two segments of wrinkle with (10°, 20°) orientation. (**h**–**j**) The snapshots in growth simulation of graphene corresponding to schematic (**g**); (**k**,**l**) top view and side view of the final structure corresponding to schematic (**g**). (**m**) Schematic of the case which has three segments of wrinkle with (-5°, 10°, -5°) orientation; (**n**–**p**) the snapshots in growth simulation of graphene corresponding to schematic (**m**); (**q**,**r**) top view and side view of the final structure corresponding to schematic (**m**). (**s**) Schematic of the case which has three segments of wrinkle with (-5°, 10°, 20°) orientation; (**t**–**v**) the snapshots in growth simulation of graphene corresponding to schematic (**s**); (**w**,**x**) Top view and side view of the final structure corresponding to schematic (**s**).

https://doi.org/10.1038/s41563-023-01632-y

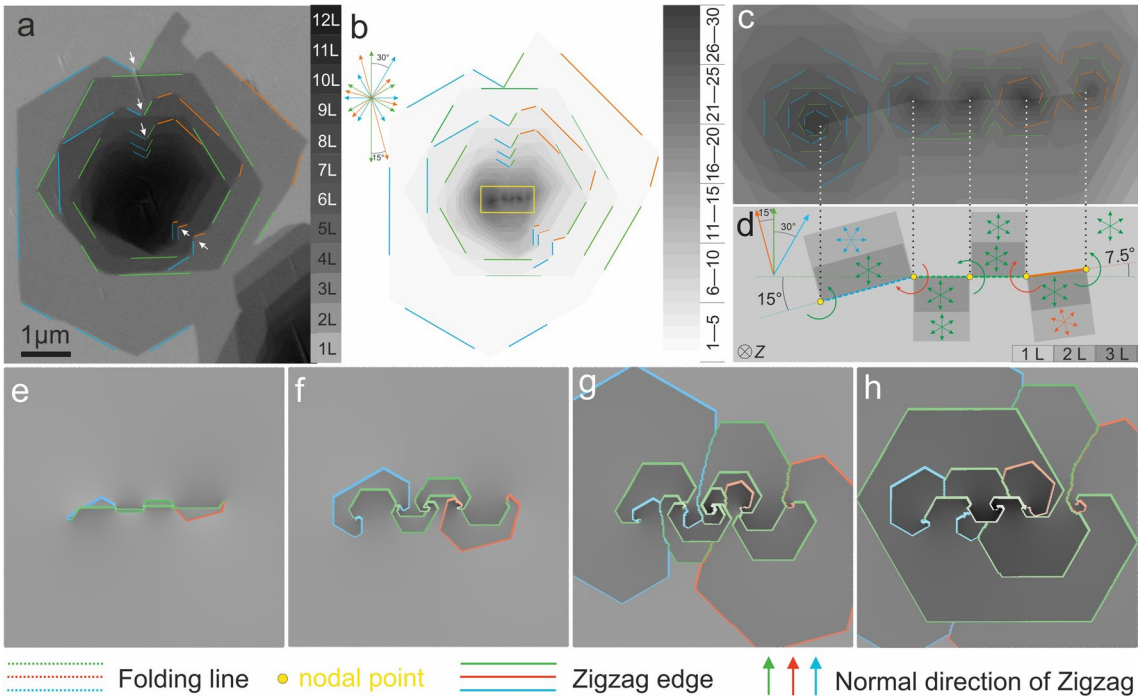

Extended Data Fig. 9 | Reverse inference graphene spiral structure. The ESEM image (**a**) shows a complex shaped multi-layer graphene. The brightness in the secondary electron image changes with each additional layer. (**b**) Reproduced the shape of multi-layer graphene using GSs coalescence, and (**c**) is a zoom-in of local brightness topography over the region indicated by the yellow window in panel (**b**). (**d**) Schematic representation of initial state (**c**) using origami-kirigami like graphene folds. The number of layers can be abstracted by comparing the contrast in the images with the contrast legend in the (**a**,**b**). According layout of graphene folding in (**c**), the coalescence of GSs are simulated by KMC in (**e**–**h**) and represent apparent layer-by-layer growth behaviour.

https://doi.org/10.1038/s41563-023-01632-y

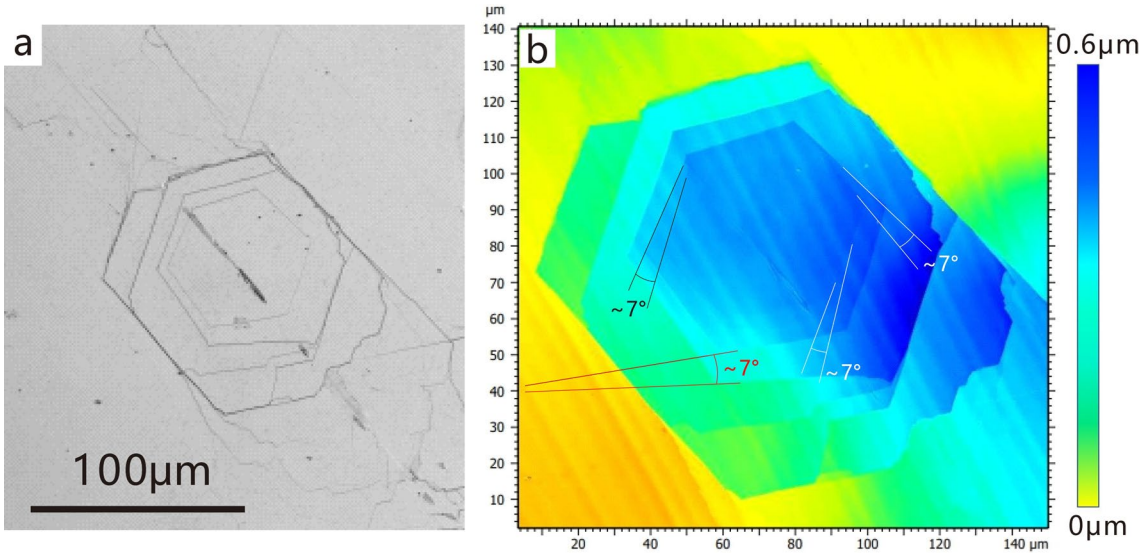

Extended Data Fig. 10 | Characterization of exfoliated graphene on Pt by confocal laser scanning microscopy (CLSM). (**a**) CLSM intensity image. (**b**) CLSM height image.